

Article

Mechanical and Thermal Properties of Aluminum Matrix Composites Reinforced by In Situ Al₂O₃ Nanoparticles Fabricated via Direct Chemical Reaction in Molten Salts

Liudmila A. Yolshina ^{1,*} , Aleksander G. Kvashnichev ¹, Dmitrii I. Vichuzhanin ²  and Evgeniya O. Smirnova ²¹ Institute of High-Temperature Electrochemistry, Ural Branch of RAS, 620990 Ekaterinburg, Russia² Institute of Engineering Science, Ural Branch of RAS, 620049 Ekaterinburg, Russia

* Correspondence: yolshina06@rambler.ru; Tel.: +7-3433745044

Abstract: The development of novel methods for industrial production of metal-matrix composites with improved properties is extremely important. An aluminum matrix reinforced by “in situ” α -Al₂O₃ nanoparticles was fabricated via direct chemical reaction between molten aluminum and rutile TiO₂ nanopowder under the layer of molten salts at 700–800 °C in air atmosphere. Morphology, size, and distribution of the in situ particles, as well as the microstructure and mechanical properties of the composites were investigated by XRD, SEM, Raman spectra, and hardness and tensile tests. Synthesized aluminum–alumina composites with Al₂O₃ concentration up to 19 wt.% had a characteristic metallic luster, their surfaces were smooth without any cracks and porosity. The obtained results indicate that the “in situ” particles were mainly cube-shaped on the nanometer scale and uniform matrix distribution. The concentration of Al₂O₃ nanoparticles depended on the exposure time and initial precursor concentration, rather than on the synthesis temperature. The influence of the structure of the studied materials on their ultimate strength, yield strength, and plasticity under static loads was established. It is shown that under static uniaxial tension, the cast aluminum composites containing aluminum oxide nanoparticles demonstrated significantly increased tensile strength, yield strength, and ductility. The microhardness and tensile strength of the composite material were by 20–30% higher than those of the metallic aluminum. The related elongation increased three times after the addition of nano- α Al₂O₃ into the aluminum matrix. Composite materials of the Al–Al₂O₃ system could be easily rolled into thin and ductile foils and wires. They could be re-melted for the repeated application.

Keywords: metal-matrix composite; aluminum; nano-alumina; molten salt synthesis; mechanical properties



Citation: Yolshina, L.A.; Kvashnichev, A.G.; Vichuzhanin, D.I.; Smirnova, E.O. Mechanical and Thermal Properties of Aluminum Matrix Composites Reinforced by In Situ Al₂O₃ Nanoparticles Fabricated via Direct Chemical Reaction in Molten Salts. *Appl. Sci.* **2022**, *12*, 8907. <https://doi.org/10.3390/app12178907>

Academic Editors: Suzdaltsev Andrey and Oksana Rakhmanova

Received: 10 August 2022

Accepted: 2 September 2022

Published: 5 September 2022

Publisher’s Note: MDPI stays neutral with regard to jurisdictional claims in published maps and institutional affiliations.



Copyright: © 2022 by the authors. Licensee MDPI, Basel, Switzerland. This article is an open access article distributed under the terms and conditions of the Creative Commons Attribution (CC BY) license (<https://creativecommons.org/licenses/by/4.0/>).

1. Introduction

Metal-matrix composites based on aluminum and its alloy have been the subject of great scientific and practical interest over the last decades [1,2]. The reason is the possibility to obtain lightweight metallic materials with unique properties (enhanced hardness, ductility, elastic modulus, and many others) by combining the advantages of constructional metals with the merits of filler materials. Metal-matrix composites based on aluminum and aluminum-metal-matrix composite alloys (AMMC) are promising for aerospace, military, automobile, and electronic areas because of their low density, high specific stiffness, strong wear resistance, reduced thermal expansion coefficient and high thermal conductivity [1,2]. These materials sustain their stability characteristics over a wide temperature range, have high electrical and thermal conductivities, and low sensitivity to surface defects [3–5].

AMMCs are fabricated both by ex situ synthesis (e.g., liquid ingot casting and powder metallurgy), where reinforcement powder particles are added to the metal melt, and by in situ synthesis (e.g., exothermic dispersion, reactive hot pressing, reactive infiltration, and

direct melt reaction), where particles are directly synthesized in the metal melt [6–12]. The reinforcement in AMMCs can have a form of continuous/discontinuous fibers, whiskers, or particulates. The most frequently applied fillers are ceramic ones such as alumina, silicon carbides or nitride, carbon fiber materials, or graphene [13,14].

At present, researchers focus on the possibility of introducing the above-mentioned ceramic additives in the form of nanoparticles into the aluminum matrix. When moving to nanoscale hardeners, we have the opportunity to obtain an entirely new class of lightweight materials with increased specific strength, plasticity, and crack resistance. The mechanisms of deformation and fracture in aluminum–alumina composite materials reinforced by nanosized alumina particles can be fundamentally different from those in classical aluminum alloys.

There are some problems arising in the synthesis of Al–Al₂O₃ composites: inhomogeneity of the distribution of oxide nanocrystals in the volume of the metal matrix; the tendency of nano-objects to agglomeration inside the matrix (1–3 μm); low wettability of oxide particles by molten aluminum (lattice consistency of the reinforcing phase and aluminum), and degradation of oxide materials (chemical, mechanical, etc.).

The mechanical addition of alumina particles into the metal melt by means of powder metallurgy [15–17] results in the interface pollution, poor wetting ability, and mechanical properties. The composites synthesized via the ex situ methods have high porosity and a lot of cracks. They are characterized by the appearance of “soft” and “hard” phases [17] because of the difference in aluminum particles’ concentration and agglomeration [15]. Hence, the mechanical properties of composites produced by powder metallurgy methods can vary greatly.

Selective laser melting can be used for the creation of advanced ball-milled Al–Al₂O₃ nanocomposites with a two-fold increase in Vickers micro-hardness compared to the initial Al [18]. The mechanical properties of Al–nano Al₂O₃ produced by ball-milling and hot-pressing under uniaxial pressure of 50 MPa were improved due to the utilization of nano-sized reinforcement particles [19]. To date, the compaction of several layers of aluminum foil and aluminum oxide powder, followed by rolling from 2 to 20 times, is another promising method of composite materials’ fabrication [20–22]. As a result, layered laminated Al–Al₂O₃ composite structures are formed. The uneven distribution of aluminum oxide particles in the aluminum matrix, as well as the significant agglomeration of oxide particles [21], are the main problems of the laminated composite production that cause the uneven properties of the composite. Such defects are usually eliminated by increasing the number of rolling cycles. In addition, the non-isomorphism of the composites’ properties is also a problem.

Sometimes, both powder metallurgy and rolling are combined for the synthesis of composites, which makes it possible to obtain Al–Al₂O₃ composites with a better distribution of dispersing particles [23].

Direct reaction synthesis (DRS) refers to the process in which reactant powders or compacts of reactant powders are directly added to molten metal, and ceramic reinforcing particles are formed in situ through the exothermic reaction between reactants or between the reactant and the component of the melt. During the in situ process, the reinforcement phases formed in the matrix metal by direct chemical reactions are thermodynamically stable, free of surface contamination, and disperse more uniformly. These factors lead to the stronger particle–matrix bonding at the “in-situ” process.

DRS in situ synthesis can be applied as a commercial method because of its simplicity, low cost, and near-net-shape-forming capability. The biggest problem of the traditional DRS method is the necessity of a long mixing time at a high temperature, which causes the agglomeration of small initial particles [24,25]. The introduction of alumina to the molten aluminum matrix by the “in situ” process was proved by different independent physical–chemical methods such as XRD, Raman spectroscopy, and others [26].

Nowadays, synthesizing Al–Al₂O₃ nanocomposites is an important practical and fundamental task in the field of inorganic chemistry. There is a very high need to create

a high-tech method for the synthesis of non-porous aluminum–alumina nanocomposites with improved mechanical properties.

The novelty of the present work is that the aluminum matrix was reinforced by “in situ” perfectly wetted and well-distributed Al_2O_3 nanoparticles, formed via a direct chemical reaction between molten aluminum and rutile TiO_2 nanopowder under a molten salt layer at 700–750 °C in air atmosphere. The microstructure and mechanical properties of the composites were investigated by XRD, Raman spectroscopy, SEM, and tensile testing.

This research aims to develop a method for the industrial large-scale “in situ” synthesis of aluminum-based matrix composites, reinforced with ceramic nanoparticle inclusions. These composites are formed via the reaction between molten aluminum and the salt electrolyte flux, which contains rutile TiO_2 nanopowder as the precursor. The effect of nano-alumina inclusions content on mechanical and thermal properties of the Al-nano- Al_2O_3 composite is analyzed.

2. Experimental

Titanium dioxide nanopowders were produced by electrochemical oxidation of titanium foil of 99.9 wt.% purity (“VSMPO-Avisma”, Ekaterinburg, Russia) in the chloride-nitrate melt according to the method described in detail elsewhere [27,28]. The interaction between molten aluminum and nano- and micro-oxide powders of titanium dioxide was performed in molten alkali halide media in an alumina crucible containing the mixture of alkali chlorides with a weighed portion of oxide additive. Salt mixtures of alkali chlorides with melting points lower than 700 °C, with small additions of some fluorides, were used as a base electrolyte with the concentration of titanium dioxide ranging from 0.2 to 2 wt.%. We used commercial “chemically pure” salts provided by “Lanhit” Ltd., Moscow, Russia.

The aluminum sample A95 of 99.5 wt.% purity (“Rusal”, Russia) consisted of a 1 cm high disc with a diameter strictly equal to the crucible diameter. The disc was loaded into a layer of the dry oxide–salt mixture at the bottom of the crucible. The primary admixture of technical aluminum was iron—about 0.5 wt.%. The aluminum disc was covered by a layer of dry alkali chlorides. The alumina crucible was exposed inside the vertical heating furnace at the temperatures range of 700–800 °C for 3 to 5 h. After the exposure, the liquid aluminum globule was poured into the new cold alumina crucible. After the solidification, the salt mixture was dissolved in distilled water. The aluminum composite ingot was separated and dried. Cooled to the ambient temperature, aluminum–alumina composite ingots were divided into four parts. One part was used for the determination of Al_2O_3 content in the composite, the second part was used for XRD analysis, the third one was poured with current-carrying gum, polished by six different silicon solutions using a Struers disc-finishing machine (Copenhagen, Denmark), and examined by means of scanning electron microscopy (SEM, Raman spectroscopy (Wotton-under-Edge, England, UK), microhardness testing). The fourth biggest part was remelted to form cylindrical samples for a servo-hydraulic testing machine.

The processing of the studied composites is schematically shown in Figure 1.

The structures of titanium dioxide and aluminum–alumina composite were studied by means of SEM, XRD, and Raman spectroscopy. In order to determine the material composition and the composite structure, the purity of the oxide phase was analyzed using Raman spectra by a Renishaw U 1000 micro-Raman spectrometer (UK) connected to a Leica DML microscope equipped with 50× and 100× magnification lenses. An Ar^+ laser (Cobalt model) with a wavelength of 532 nm and power output of 20 mW was used as the excitation source. The diameter of the laser spot was about 1 μm; the acquisition time was set to 20 s. The XRD analysis was performed on a «RIGAKU» DNAX 2200PC diffractometer at ambient temperature with $\text{Cu K}\alpha$ radiation. Subsequent analysis of the vibrational spectra was carried out using the embedded Wire 3.0 software (Wotton-under-Edge, England, UK); the spectral lines were approximated using the Fityk 0.9.8 curve fitting and data analysis application. The typical average spectra obtained are presented for each sample.

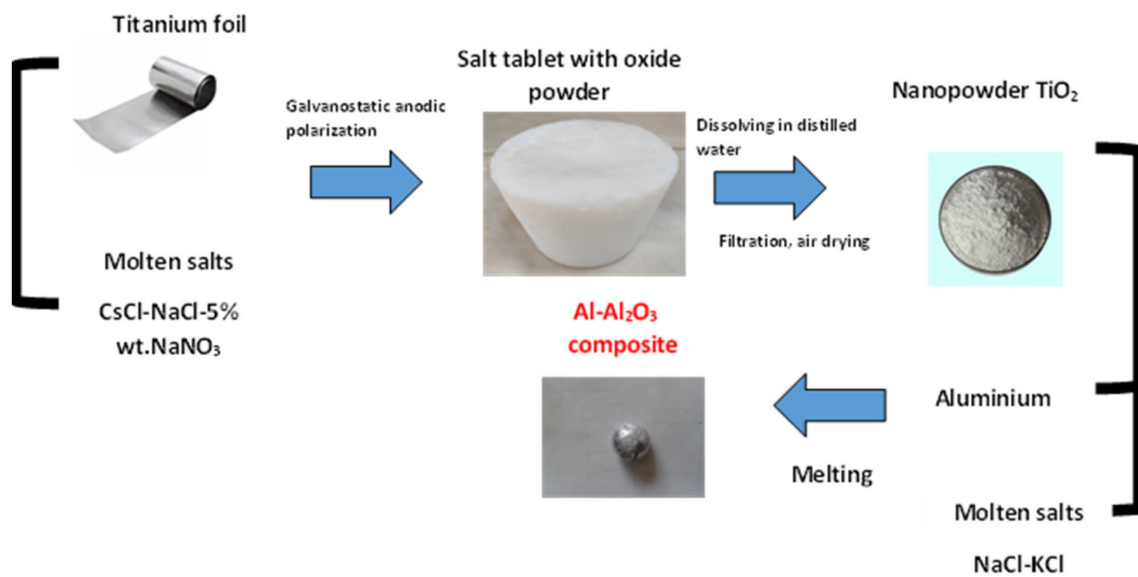
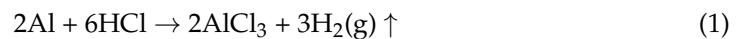


Figure 1. Processing schematic of Al/Al₂O₃ nanocomposite.

The volumetric method determined the quantitative content of aluminum oxide in the produced AMMC. Volumetric analysis was carried out by dissolving a composite sample in 30% hydrochloric acid, followed by recalculating the released hydrogen per mass of pure aluminum in the sample according to reaction (1):



The sample was then examined as follows: scanning electron microscopy (SEM) was performed using JEOL 5900LV and TESCAN MIRA3 microscopes; the sample surface was characterized by a Veeco Wyko NT 1100 optic profilometer-profilograph in the Vertical Scanning Interferometry (VSI) regime; the fatigue strength was examined by a servo-hydraulic testing machine INSTRON 8801, the sample microhardness was tested a WIN-HCU FISCHERSCOPE HM 2000 XYm system, which is designed for Martens hardness testing with the WIN-HCU software at a maximum load P from 1000 mN to 2000 mN, a loading time of 20 s, a time of exposure under loading of 15 s, and an unloading time of 20 s according to the ISO 14577 standard [29].

The characteristics measured by indentation were used for the calculation of the following parameters: the ratio of the indentation hardness to the contact elasticity modulus HIT/E^* [30], the elastic recovery $R_e = \frac{h_{\text{max}} - h_p}{h_{\text{max}}} \times 100\%$ [31], the power ratio [32], and the plasticity index $\delta_A = 1 - \frac{W_e}{W_t}$ [29] that characterizes the ability of a material to resist elastoplastic strain. Ten measurements of indentation characteristics at each load were performed. The error of measurements was determined with a confidence probability $p = 0.99$.

3. Results and Discussion

3.1. Formation of Nano-Titanium Dioxide as a Precursor

The formation of titanium nano-oxide powders as precursors of composite synthesis was carried out by electrochemical oxidation of pure titanium in a chloride-nitrate melt in an argon atmosphere [27]. The main function of the nitrate melt is corrosion protection against the aggressive environment due to the formation of dense protective oxide layers on metals. Chloride-nitrate melts allow synthesizing both dense protective coatings and nanocrystalline powders of metal oxides such as Al₂O₃, TiO₂, ZrO₂, and PbO [33,34] varying the nitrate concentration in the flux. Due to the alkali nitrates' thermal instability, the temperature range of their application is narrow, while amorphous oxides are usually

formed at low temperatures. It is necessary to synthesize oxides using salt electrolytes with higher melting points to increase the temperature of the crystalline metal oxide synthesis.

The metal oxidation in the chloride-nitrate salt melt bulk at the current densities ranging from 3 to 5 mA/cm² lead to the accumulation of significant amounts of oxide nanopowder in the bulk salt electrolyte. The chemical composition and modification of the formed oxides depended mainly on the oxidation temperature.

Despite the nanometer size of titanium dioxide crystallites (Figure 2a), the X-ray diffraction pattern contained main rutile titanium dioxide lines of 2θ angle at 27.5°, 36.16°, 39.26°, 41.32°, 44.14°, 54.42°, 56.72°, 63.44°, and 69.11° with diffraction plans (110), (101), (200), (111), (210), (211), (220), (002), and (301), respectively (JCPDS no. #88-1175) [35] (Figure 2c). The broadening of lines or a halo was not observed, which may be explained by the fact that the formed oxide particles were well-faceted cubic crystals, and not spheroids, as is often the case, which happens in the synthesis of nano-oxides by the sol-gel method. Titanium dioxide nanopowders synthesized in a molten chloride-nitrate electrolyte at the current density of 3.5 mA/cm² were characterized by a high degree of crystallinity and took the form of titanium dioxide cubes with a size up to 30 nm (Figure 2a).

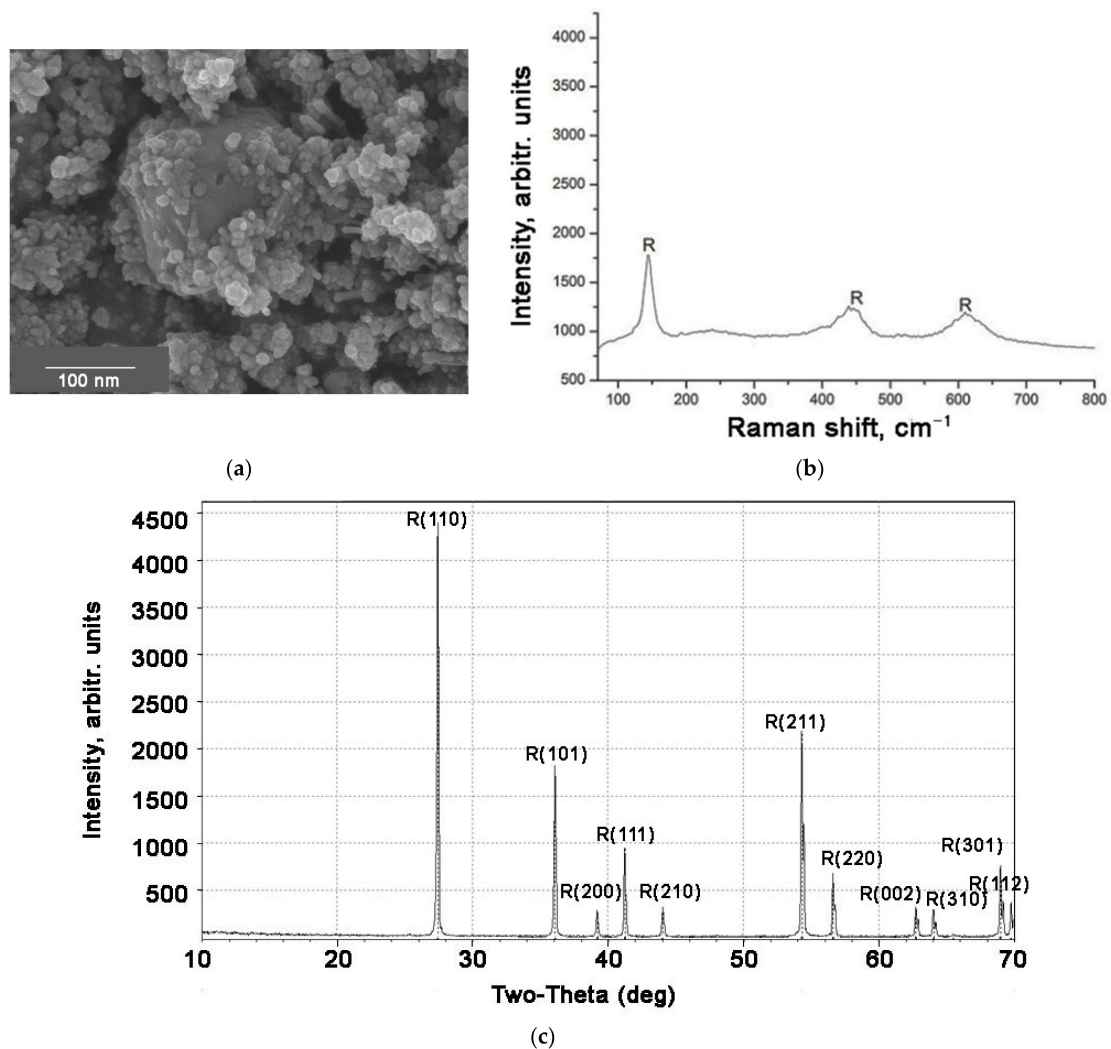


Figure 2. SEM image (a), Raman spectrum (c), and XRD pattern (b) of TiO₂ nanopowder in rutile modification synthesized in NaCl-CsCl-5% NaNO₃ at 700 °C.

According to the results of the Raman spectroscopy of the sample obtained at 700 °C, peaks characteristic for the modification of rutile TiO₂ were determined in the Raman bands: 144 cm⁻¹, 448 cm⁻¹, 612 cm⁻¹ (Figure 2b).

Further, rutile titanium dioxide nanopowder formed under the above conditions was used as a precursor.

Various industrially sol-gel methods for nano- and micro-powders production in the form of rutile and anatase were previously studied as precursors for the synthesis of the nanocomposite. However, all these nanopowders were sedimented to the bottom of the crucible and reaction (3) (Table 1) did not proceed. The titanium dioxide nanopowder in the rutile modification synthesized by the electrochemical oxidation of titanium in a chloride–nitrate melt was the only precursor with which the above reaction was successful.

Table 1. Gibbs energies of some possible reactions in the Al-TiO₂-NaCl-O₂ system.

Reaction		$\Delta G_{700\text{ }^\circ\text{C}}$	$\Delta G_{750\text{ }^\circ\text{C}}$	$\Delta G_{800\text{ }^\circ\text{C}}$
$13\text{TiO}_2 + 4\text{NaCl} = 2\text{Na}_2\text{Ti}_6\text{O}_{13} + \text{TiCl}_4(\text{g})$	(2)	333.9	326.0	318.0
$3\text{TiO}_2 + 4\text{Al} = 3\text{Ti} + 2\text{Al}_2\text{O}_3$	(3)	−437.6	−430.85	−424.0
$13\text{Ti} + 4\text{NaCl} + 13\text{O}_2 = 2\text{Na}_2\text{Ti}_6\text{O}_{13} + \text{TiCl}_4(\text{g})$	(4)	−9642.6	−9535.7	−9429.0
$3\text{TiO}_2 + 7\text{Al} = 3\text{AlTi} + 2\text{Al}_2\text{O}_3$	(5)	−643.7	−643.2	−624.7
$3\text{TiO}_2 + 13\text{Al} = 3\text{Al}_3\text{Ti} + 2\text{Al}_2\text{O}_3$	(6)	−804.8	−788.9	−773.0

3.2. Interaction between Molten Aluminum and Titanium Nanodioxide under the Layer of Molten Halides and Analysis of Interaction Products

The AMMC material dispersion reinforcement is typically achieved by casting or powder metallurgy, with the ceramic particles being introduced ex situ into a solid or liquid matrix. A new AMMC production method has been developed on the basis of the controlled “in-situ” chemical reactions; reinforcing fillers are formed during the chemical interaction between the matrix components and reactive additives [9,12]. Such AMMCs demonstrate excellent mechanical and physical properties, because coherent (i.e., having a standard atomic layer at the interface) or partially coherent interfaces are formed between the matrix and new phases that arise in “in-situ” reactions.

The uniform distribution of fine particles of alumina in the aluminum matrix was achieved by the modified method of molten salt synthesis. Molten halides (alkali or alkali-earth chlorides and/or fluorides) are the optimal reactive media for the formation of aluminum–alumina composites, as was shown in our previous papers [26,36].

The synthesis of alumina particles inside aluminum is carried out by a one-step chemical reaction of titanium dioxide with molten aluminum under the layer of molten halides in air atmosphere by reaction (3); therefore, newly formed alumina nanoparticles are perfectly wetted by the liquid metal.

Obviously, these reactions, except for the direct interaction between TiO₂ and molten sodium chloride, are thermodynamically feasible at sufficiently low temperatures of 700–800 °C. The presented process is a special case of aluminothermy.

The interaction between liquid aluminum and fine titanium dioxide particles by reactions (5) and (6) can proceed up to the formation of the intermetallic AlTi and Al₃Ti titanium aluminide compounds. The Gibbs energies of reactions (5) and (6) are more negative than that of reaction (3). It makes reactions (5) and (6) more favorable.

Titanium aluminides were not detected in the reaction product by X-ray phase analysis, Raman spectroscopy, EDS spectra of composites, and mapping sample surfaces in X-rays. Intermetallic compounds of aluminum and titanium or titanium species were not detected by means of an inductively coupled plasma optical emission spectrometer OPTIMA 4300 DV (Perkin Elmer, USA) after dissolving the resulting composite in hydrochloric acid. Thus, it can be argued that the interaction occurred according to the mechanism described above by reaction (3).

The reason for such a result is the appearance of a side reaction (4) in the system. The interaction between titanium atoms, sodium chloride, and gaseous oxygen according to reaction (4) resulted in the formation of Na₂Ti₆O₁₃ nanowires and nanorods, which was

experimentally proved [37]. The value of Gibbs energy of this reaction is 15 times greater than that of all other reactions.

The composites obtained in this way were non-porous with a characteristic metallic luster (Figure 3). They exhibited high electrical conductivity and are excellently suited for mechanical processing. It was experimentally proved that the aluminum oxide content did not change from the surface of the aluminum drop to its center. The density of the obtained composite averaged 2.6977 g/cm^3 , which is very close to that of pure aluminum (2.6989 g/cm^3), and indicates the absence of porosity in the composite, which is typical for such samples obtained by traditional methods.

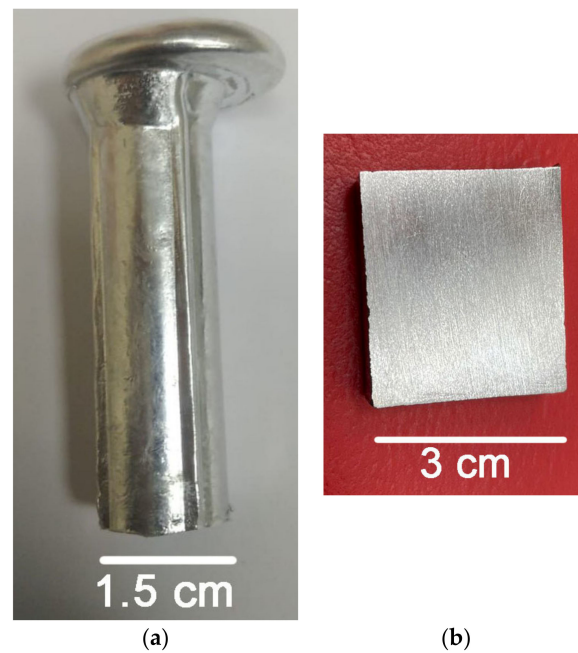


Figure 3. Optic photo of the ingot (a) and cross-section (b) of Al-Al₂O₃.

According to the X-ray diffraction data, the thus obtained material was composed of Al and α -Al₂O₃ [36].

Raman spectra of the oxide inclusions were collected from several crystals inside the aluminum matrix. The average spectrum of the oxide inclusion is presented in Figure 4. It is obvious that this spectrum was a standard spectrum of α -Al₂O₃ with the characteristic bands at 378 cm^{-1} , 417 cm^{-1} , 430 cm^{-1} , 448 cm^{-1} , 576 cm^{-1} , 644 cm^{-1} , and 749.5 cm^{-1} [38]. It confirmed the XRD data about the synthesis of α -Al₂O₃ inside the aluminum matrix [36].

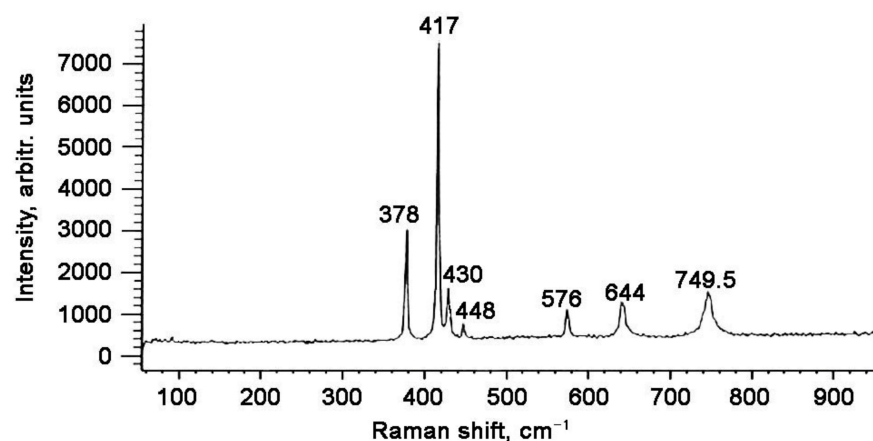


Figure 4. Raman spectrum of the oxide inclusion inside the Al matrix.

Micro- and nanosized inclusions of aluminum oxide were also clearly visible in the micrographs in the optic microscope (Figure 5a) and in backscattered electrons in a scanning electron microscope (Figure 5b,c). The EDS spectrum of inclusion showed the content of aluminum and oxygen in the stoichiometric ratio of Al_2O_3 ; inclusions of aluminum oxide had sizes close to 100 nm.

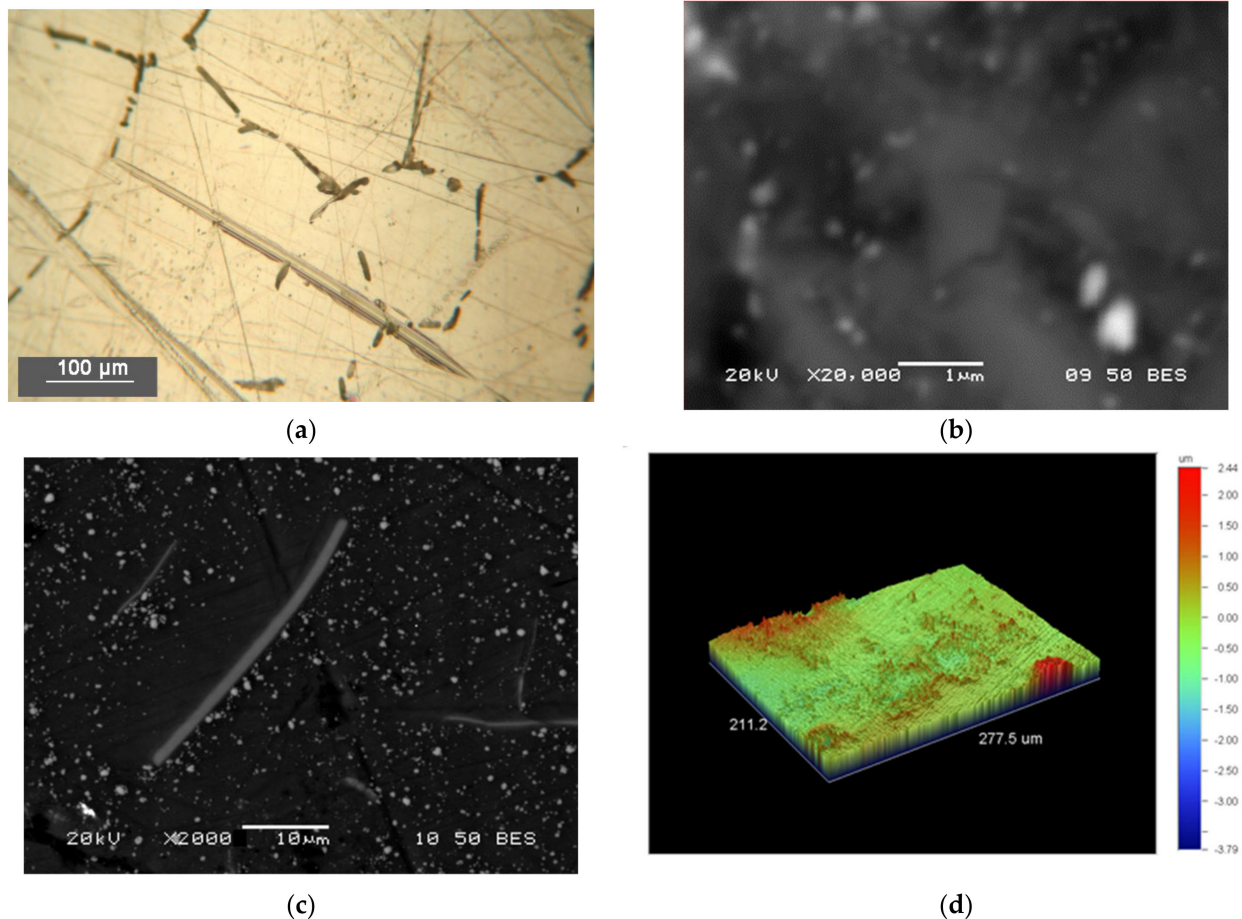


Figure 5. Optic photo of the cross-section of Al- α - Al_2O_3 composite (a) ($\times 40$); BES images of Al- α - Al_2O_3 composite (b,c); 3D image of Al- α - Al_2O_3 composite (d).

A very uniform distribution of oxide inclusions inside aluminum grains of the cross-section of Al- α - Al_2O_3 composite is presented in Figure 6.

Inclusions in the form of long rods were crystals of iron aluminide Al_3Fe (Figure 6), which were present in the starting aluminum as an admixture. According to the phase measurements of the cross-section of this sample, the Al area is 97.5%, Al_3Fe -1.4%, and Al_2O_3 -1.2%. The 3D image of the cross-section of AMMC (Figure 5d) also shows a uniform distribution of alumina nanoparticles inside the grain of the aluminum matrix.

To prove the possibility of finding nanoparticles mainly inside the grain rather than at the grain boundary, as would be expected from classical considerations, we calculated the value of the critical nucleus (r_c) during the crystallization of aluminum using well-known Formula (7) [39]:

$$r_c = \frac{2\sigma T_{12}M}{Q_{12}\Delta T\rho'} \quad (7)$$

where σ is the surface tension of the metal melt; T_{12} is the melting point of the metal; M is the molecular weight; Q_{12} is the heat of crystallization (heat of fusion); ΔT is the supercooling of the melt, at which the nucleation of the crystallization center occurred; ρ is the density of the metal.

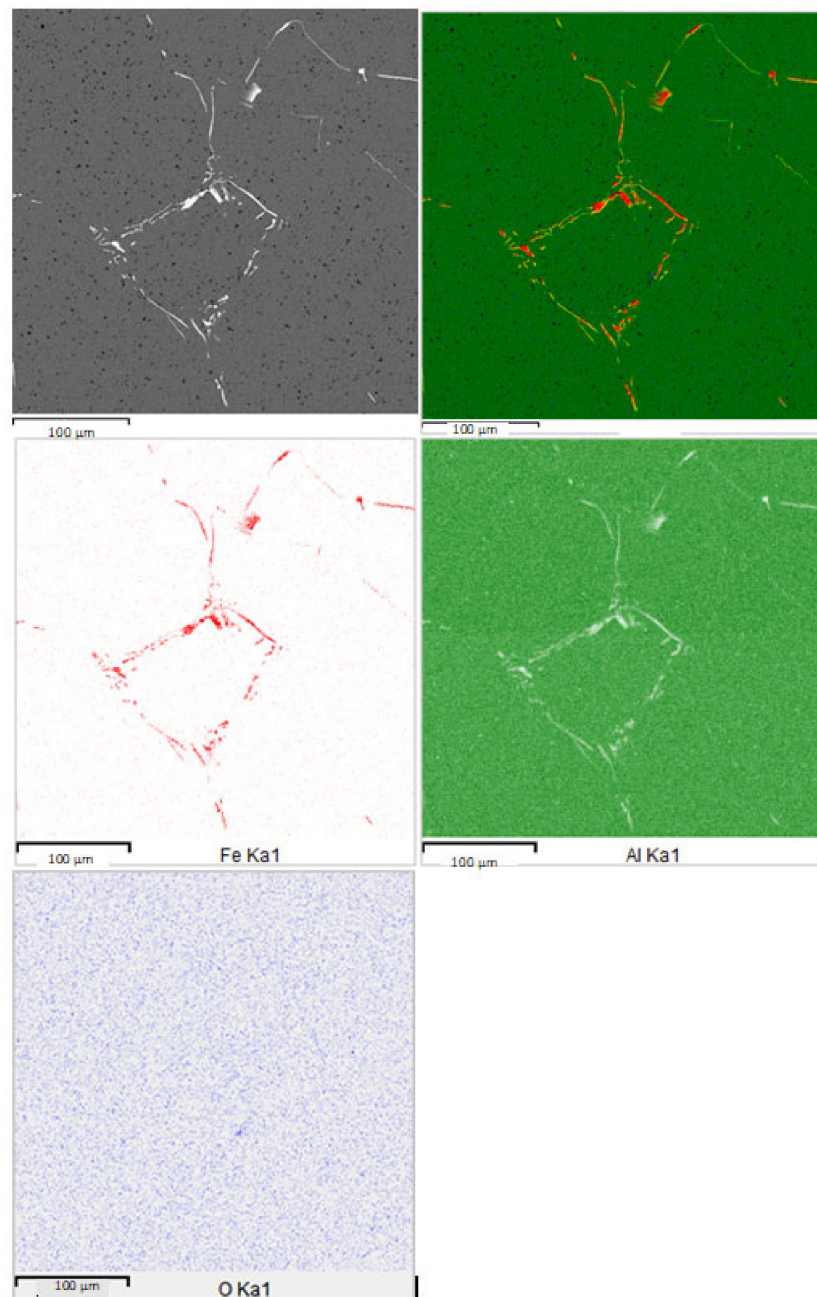


Figure 6. Elemental distribution map of the Al-1.2% Al₂O₃ composite cross-section.

As a result, the value of the radius of the critical nucleus of Al₂O₃ was $r_c = 108.33$ nm.

Thus, the size of the critical nucleus was three times larger than the initial size of the nanoparticles (30 nm), and the calculated value of synthesized α - alumina in the aluminum matrix was very close to the experimental one, which varied from 100 to 150 nm.

Thus, it can be assumed that nano- α aluminum oxide formed as a result of the chemical interaction between fused aluminum and nanopowder of titanium dioxide and was not grouped along the grain boundaries but was uniformly distributed in the volume of the aluminum grain (Figures 5 and 6), which is a favorable factor in assessing the mechanical properties of the composite.

The composite samples were dissolved in hydrochloric acid HCl solution to determine the quantitative content of aluminum oxide in the produced AMMCs using the volumetric method. The concentration of Al₂O₃ in the composite was determined by the difference in hydrogen evolution.

The data in Table 2 elucidates that an increase in the exposure time and concentration of titanium dioxide in the melt leads to an increase in the mass fraction of aluminum oxide in the composite. However, when the titanium dioxide concentration increased significantly above 1% and exposure time was up to 9 h, it was not possible to obtain samples with a reinforcing phase concentration of more than 19%. A slight decrease in the mass fraction of aluminum oxide in the composite caused by an increase in temperature to 750 °C could be associated with the interaction between atomic titanium and a salt flux, which resulted in the formation of sodium titanate.

Table 2. The influence of the concentration of TiO₂ precursor, temperature, and exposure time on the concentration of Al₂O₃ inside the obtained Al-Al₂O₃ composite.

% TiO ₂ Added	T Exposure, h	T Interaction, °C	% Al ₂ O ₃ in the Ingot
0.5	3	700	7.8 ± 0.2
0.5	5	700	13.5 ± 0.3
0.5	3	750	4.6 ± 0.2
0.5	5	750	13.0 ± 0.3
1.0	3	700	8.2 ± 0.2
1.0	5	700	18.4 ± 0.2
1.0	3	750	8.7 ± 0.3
1.0	5	750	10.1 ± 0.3

As can be seen from Table 2, we varied the concentration of aluminum oxide of AMMC not by introducing a certain amount of aluminum oxide into the aluminum matrix, but by changing the synthesis time and temperature. The content of aluminum oxide formed by the reaction (3) did not depend on the titanium dioxide weight. Titanium dioxide was a necessary seed for the formation of aluminum oxide in the composite; when interacting in a salt melt, it formed sodium hexatitanate nanofibers in stoichiometric amounts [37].

3.3. Thermal Analysis of Composite Al-Nano-Al₂O₃

Thermal analysis of Al-Al₂O₃ composites was measured by a thermal analyzer STA 449C Jupiter, NETZSCH at a heating rate of 10 K/min, the temperature determination error was <1.5 K. Synchronous analysis of samples of aluminum–nano-alumina composites was carried out by differential scanning calorimetry (DSC) and thermogravimetry as a function of temperature in air atmosphere. In the first case, the sample was heated to temperatures up to 723 °C, cooled and, without removing the sample from the crucible, heated repeatedly to the same temperatures, and then the sample was heated to the temperature of 800 °C. The samples of the initial aluminum and studied composites exhibited congruent melting, since the melting peaks were reproduced during repeated cooling and heating cycles, while the lines were expressed in one DSC anomaly with the same areas during each repeated cooling/heating cycle. The onset points changed no more than 0.3 °C, hence the maximum temperatures, indicating the termination of the melting process of the samples, differed slightly and fluctuated in the range of 669.9–671.4 °C (Table 3).

Table 3. Onset points, melting temperatures, and Gibbs energies of melting of Al-Al₂O₃ samples.

Nº	Al ₂ O ₃ , wt. %	T _{ons} , °C	T _m , °C	ΔG, J/g
1	0	660.3	669.9	−10.63
2	7.8	660.5	671.4	−10.55
3	18.4	660.6	669.4	−10.8
4	4.6	660.2	668.4	−10.91

This phenomenon illustrates the property of peak reproducibility (Figure 7), which is a reflection of the reversibility of the phase transition during cooling and subsequent heating. The closeness of the value for the obtained composites to the parameters of the original metal can be primarily due to the indicators of the wettability of the dispersed oxide nanophase by aluminum. The data obtained by the thermogravimetry simultaneously with the differential scanning calorimetry also revealed that the thermal stability of the obtained composite materials was close to pure aluminum. The recorded change in the mass of the aluminum was equal to 0.74% and that in the composite samples during three heating and cooling cycles did not exceed 0.37%. Such an insignificant change in the mass of the sample during measurements, accompanied by the appearance of lines attributed to endothermic anomalies during DSC, directly indicated the presence of the process, which is a first-order phase transition with a high reproducibility index.

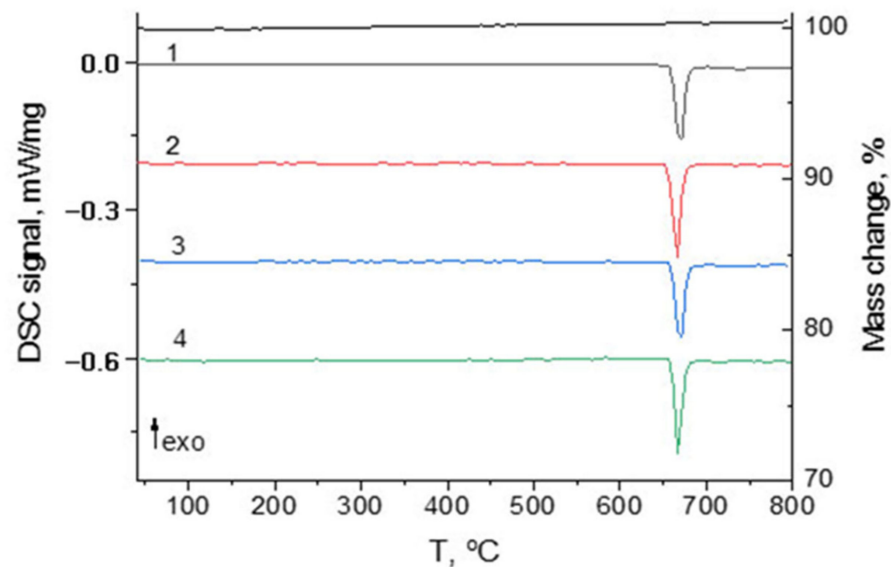


Figure 7. DSC curves (left) of initial aluminum (1), AMMCs with 7.79% (2), 18.4% (3), and 4.61% (4) of Al_2O_3 .

3.4. Measurement of Mechanical Properties of Composite Al-Nano- Al_2O_3

Experimental methods to study mechanics of deformable “Al-nano- α -alumina” composites included hardness studies and tensile testing of the material with data registration in the form of “stress-strain” curves. For the in-depth mechanical studies, samples with an aluminum oxide concentration of 10 and 14 wt.% were selected.

The instrumented indentation data on the specific features of Al and Al- Al_2O_3 behavior under elastoplastic strain are given in Table 4. It is evident that the “in situ” implementation of uniformly distributed nano- α Al_2O_3 (10 and 14 wt.%) into the aluminum matrix decreased in the maximum and residual indentation depth h_{max} and h_{p} and increased in the Martens hardness H_{M} and the indentation hardness at all loads H_{IT} . Such simultaneous change in the characteristics h_{max} , h_{p} , H_{M} , H_{IT} , W_{e} , and W_{t} measured in the indentation process is commonly caused by the material hardening and mainly is observed in aluminum composites with uniformly distributed alumina nanopowders [40–42]. In particular, for the samples “Al- nano-alumina”, an average increase in H_{IT} was nearly 20–25%. Contact elasticity modulus E^* decreased for Al-14% Al_2O_3 composite at the load 1000 mN and did not change for all other composites.

The AMMC was characterized by higher resistance to elastoplastic strain as evidenced by an increase in the calculated parameters R_{e} by factor 1.22–1.52, H_{IT}/E^* by factor 1.2–1.5, and H_{IT}^3/E^{*2} by the factor 2.1–2.7 (Table 5). The plasticity index δ_{A} did not change at the increased hardness and remained relatively high in the range of 0.972–0.982.

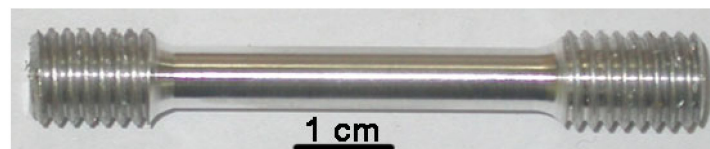
Table 4. Results of microindentation to the surface of Al and Al-Al₂O₃ samples at different maximum indenter loads P.

	P, mN	h _{max} , μm	h _p , μm	HM, MPa	H _{IT} , MPa	E*, GPa	W _t , μJ	W _e , μJ
Al in	1000	11.20 ± 0.28	11.03 ± 0.85	310.7 ± 2.8	332.6 ± 0.3	91.1 ± 2.7	3.9 ± 0.2	0.1 ± 0.005
Al in	2000	16.05 ± 0.35	15.83 ± 0.91	301.7 ± 1.4	323.2 ± 4.5	97.4 ± 3.1	11.0 ± 0.6	0.2 ± 0.005
Al-10% Al ₂ O ₃	1000	10.25 ± 0.7	10.07 ± 0.7	372.8 ± 3.0	398.4 ± 3.2	91.7 ± 5.5	3.7 ± 0.4	0.1 ± 0.005
Al-10% Al ₂ O ₃	2000	14.48 ± 0.5	14.22 ± 0.6	374.2 ± 4.4	399.9 ± 7.4	92.7 ± 3.1	9.7 ± 0.6	0.3 ± 0.005
Al-14% Al ₂ O ₃	1000	10.18 ± 0.04	9.95 ± 0.003	381.7 ± 1.1	407.0 ± 7.7	74.8 ± 1.1	3.5 ± 0.1	0.1 ± 0.005
Al-14% Al ₂ O ₃	2000	15.07 ± 0.24	14.85 ± 0.24	343.7 ± 1.0	367.7 ± 1.1	94.5 ± 2.2	10.6 ± 0.1	0.3 ± 0.005

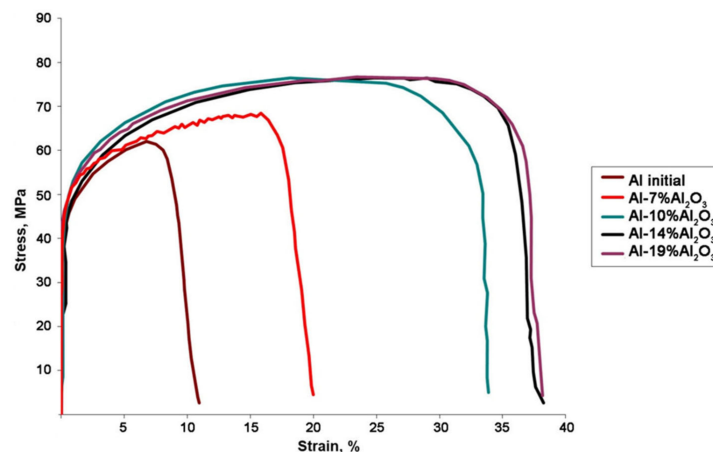
Table 5. Elastic recovery R_e, ratios H_{IT}/E* and H_{IT}³/E*², and plasticity δ_A at different maximum indenter loads P for the surface of Al and Al-Al₂O₃ samples.

	P, mN	R _e , %	H _{IT} /E*	H _{IT} ³ /E* ²	δ _A
Al in	1000	1.47	0.00365	0.00000443	0.974
Al in	2000	1.34	0.00332	0.00000356	0.982
Al-10% Al ₂ O ₃	1000	1.80	0.00434	0.00000752	0.973
Al-10% Al ₂ O ₃	2000	1.80	0.00434	0.00000744	0.969
Al-14% Al ₂ O ₃	1000	2.24	0.00544	0.0000120	0.972
Al-14% Al ₂ O ₃	2000	1.58	0.00389	0.00000557	0.972

Mechanical tensile tests of aluminum–aluminum oxide composite samples were carried out in order to determine the strength and plastic properties. The tests were carried out in accordance with RF GOST 1497-84 on IV type samples (Figure 8).

**Figure 8.** Typical Al-Al₂O₃ sample for stress–strain tests.

Typical room temperature stress–strain curves of the aluminum–alumina composites reinforced with varying alumina content are shown in Figure 9.

**Figure 9.** Typical stress–strain curves of the aluminum–alumina composites reinforced with varying alumina content.

It is evident that the yield strength did not increase with the increase of nano- α -alumina content up to 14 wt.% in the composite (Figure 10). This is in opposition to conclusions drawn in [43] that the increase in tensile strength was observed only up to α - Al_2O_3 concentrations of about 5 wt.% and the tensile strength decreased at other concentrations. The composites with an addition of 7–14 wt.% of α - Al_2O_3 possessed tensile strengths of 67.56 and 78.16 MPa, which were 1.10 and 1.27 times greater than that of the aluminum matrix sample (61.38 MPa). As can be seen from Figure 8, a further increase in the content of aluminum oxide in the composite to 19 wt.% neither improved, nor worsened, the mechanical properties of the composite. Thus, it can be considered that the aluminum oxide concentration of 14 wt.% was optimal from the point of view of the combination of all properties.

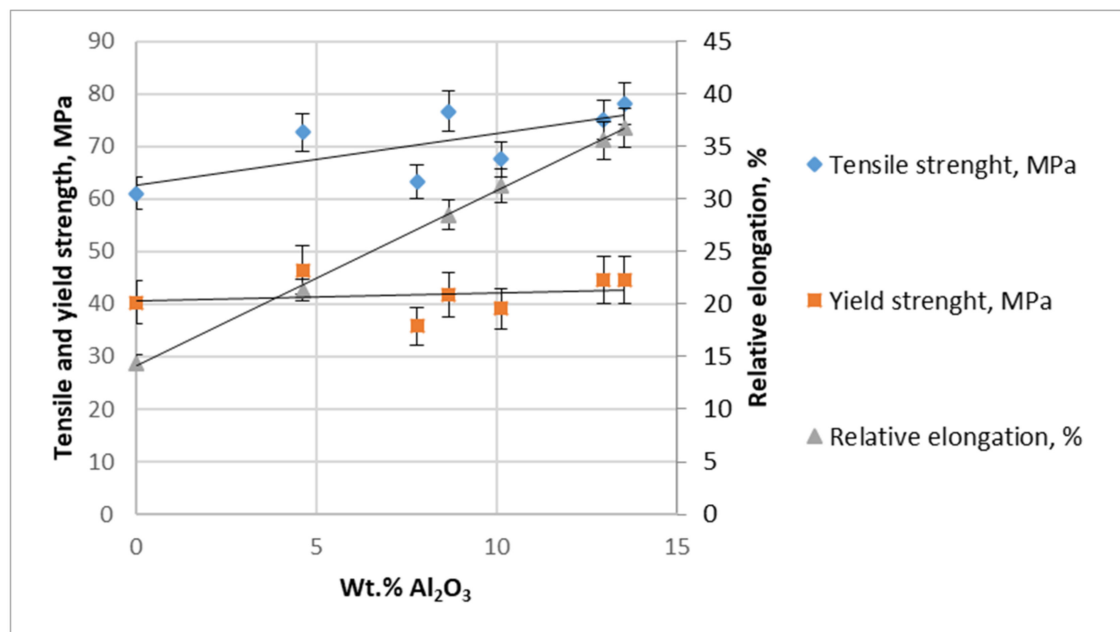


Figure 10. Dependence of tensile and yield strengths of AMMCs on the alumina concentration.

A great simultaneous increase in the sample elongation accompanied this strong improvement of tensile strength. At the same time, significant hardening was accompanied by the elongation of the samples with the addition of 7–14 wt.% of α - Al_2O_3 , which increased from 1.64 to 3.06 times with the greater addition of alumina and reached values of 21.32% and 39.77%, compared with 13% for pure aluminum. This means that the hardness, elasticity, and ductility of the aluminum-nano- α - Al_2O_3 composite improved simultaneously according to the oxide concentration with uniformly distributed α - Al_2O_3 nanoparticles inside the aluminum grains. Commonly, improving the hardness of materials leads to brittle deformation, however, the addition of up to 14 wt.% of nano- α -alumina into the aluminum matrix allows increasing simultaneously the strength, hardness, ductility, and elasticity of the resultant aluminum-nano- α - Al_2O_3 composite.

Figure 11 shows SEM images of the tensile fracture surfaces of Al- Al_2O_3 nanocomposites. The fracture mode of the initial matrix Al is predominantly not ductile, with several dimples all over the surface. As shown in Figure 11b, 14 wt.% nano Al_2O_3 -reinforced composite also displayed dimples similar to the Al matrix, except that the length and depth scale of the dimples was very different. No cracks on the fracture image of Al- nano- α Al_2O_3 nanocomposite were observed at tensile strength tests.

When the Al_2O_3 content in the composite was increased, the number and depth of the dimples decreases significantly, and the dimples' size increased at least three times, leading to a very ductile type of failure. This three-fold increase in the length of the cracks was in excellent agreement with the three-times-increased elongation of AMMC under

room temperature stress–strain tests. As seen in Figure 11b, nanoparticles of α -alumina did not agglomerate in the aluminum matrix and were uniformly distributed even after tensile strength tests. Cracks or porosity were not observed because of the very uniform distribution of α -Al₂O₃ nanoparticles in the aluminum matrix.

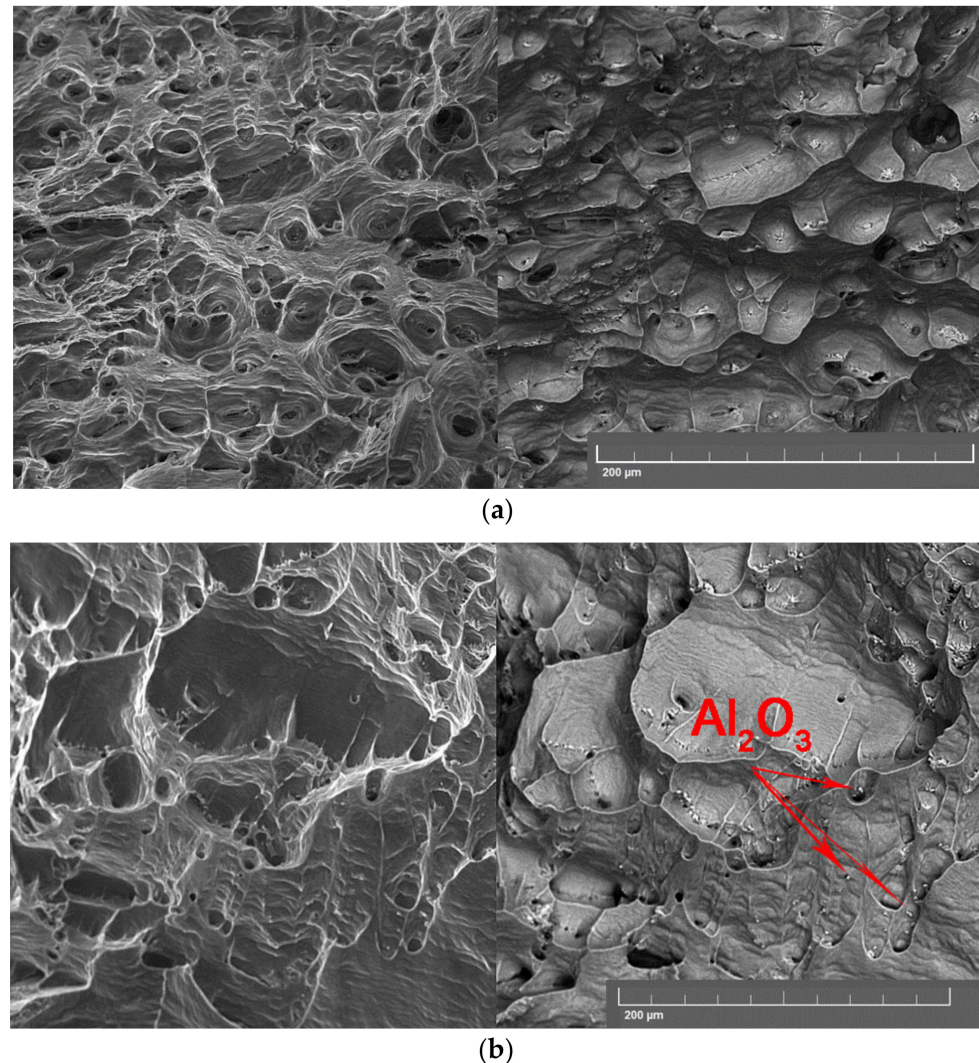


Figure 11. Fracture morphologies of Al (a) and AMMC with 14 wt.% of Al₂O₃ (b) after room temperature stress–strain tests.

3.5. Strengthening Mechanism of Al-Al₂O₃ Nanocomposites

The strengthening mechanism of Al-Al₂O₃ nanocomposites can be described by the strengthening of fine nanoparticles. Fine Al₂O₃ particles can act throughout the matrix as barriers to the dislocations and thus the elevated mechanical properties may significantly improve the hardness and ductile properties of the composites compared to the base alloy. The contributions of different strengthening mechanisms were estimated according to well-known formulas [43] (Table 6).

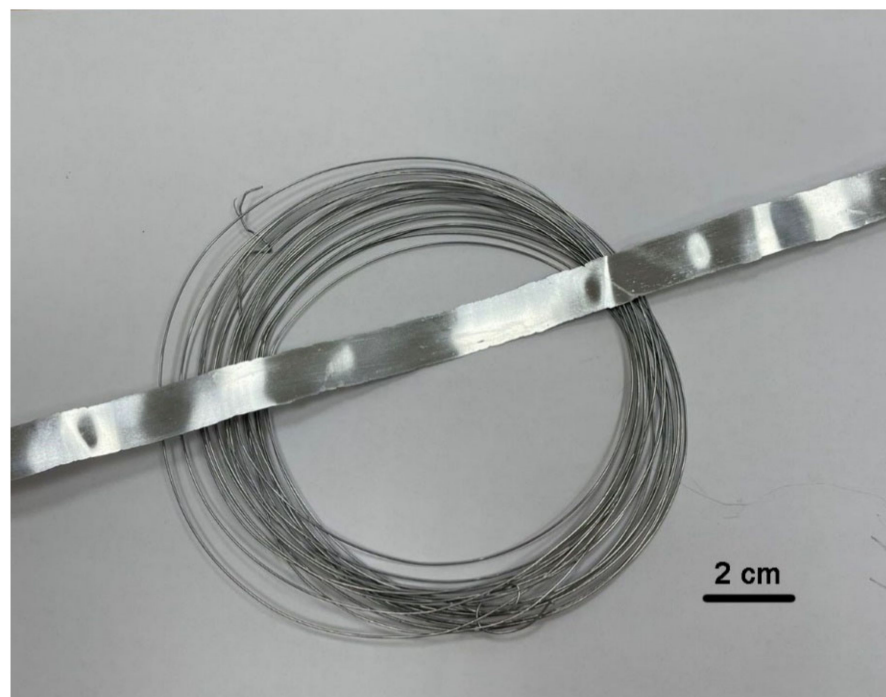
The ultra-hard α -Al₂O₃ nanoparticles in the Al matrix acted as barriers to the motion of dislocations generated in the matrix. The higher particle density caused the Orowan strengthening, which is the main influence according to Table 6. It is obvious that the experimental values were much closer to the sum of the load transfer ($\Delta\sigma_{\text{load}}$) and Orowan strengthening ($\Delta\sigma_{\text{Orowan}}$). The yield strength of the composites increased mostly because of the Orowan strengthening.

Table 6. Contributions of different strengthening mechanisms to the yield stress of Al- nano-Al₂O₃ composites.

Al ₂ O ₃ , wt. %	$\Delta\sigma_{load}$, MPa	$\Delta\sigma_{Orowan}$, MPa	$\Delta\sigma_{CTE}$, MPa	$\Delta\sigma_{theor}$, MPa	$\Delta\sigma_{load} + \Delta\sigma_{Orowan}$, MPa	$\Delta\sigma_{exp}$, MPa
7.0	0.9763	35.7268	4.4312	41.1343	36.70314	35.76
8.7	1.1948	36.4985	5.76531	43.4585	37.69324	41.69
10.1	1.1908	37.4905	3.4322	42.1135	38.68129	39.08
13.0	2.0617	44.6348	4.6656	51.3621	46.69649	44.58
14.0	2.1555	45.4353	5.6504	53.2413	47.59082	44.56

However, an increased addition of α -Al₂O₃ nanoparticles up to 14 wt.% did not lead to the agglomeration of the reinforcement, and we did not observe any subsequent degradation of the hardness values as opposed to Srivastana et al. and Su et al. [1,7]. Further increase in the concentration of highly dispersed α -Al₂O₃ nanoparticles up to 19 wt.% did not result in any hardness improvements as compared to the composite containing 14 wt.% of α -Al₂O₃, but we did not observe any deterioration in the hardness. The concentrations above 19 wt.% Al₂O₃ in the composite were not produced by our method. The strengthening from fine nanoparticles can describe the strengthening mechanism of Al-Al₂O₃ nanocomposites. Fine Al₂O₃ particles spread throughout the matrix can act as barriers to the dislocations, and thus mechanical properties of composites (hardness and ductile properties) are improved as compared to the base alloy.

The increase in hardness and strength (approximately 1.2–1.3 times) of the new composite material compared to the original aluminum is explained by the inclusion of α -Al₂O₃ particles into the aluminum matrix. The α -Al₂O₃ particles are in their strongest allotropic corundum modification, which has a hardness close to that of a diamond. An unusual increase in the relative elongation of the composite by a factor of three makes it possible to roll up to 15 μ m thick foil on conventional rolling equipment with a deformation of about 500%, as well as to draw 0.2 mm thick wire from Al-Al₂O₃ nanocomposites (Figure 12).

**Figure 12.** Optic images of 15- μ m-thick foil and 0.6-mm-diameter wire of Al-Al₂O₃ nanocomposite.

4. Conclusions

Nanocomposite Al- α -nano-Al₂O₃ materials were synthesized via the chemical interaction between a salt melt containing rutile TiO₂ nanopowder and molten aluminum under the layer of molten halides in air atmosphere at the temperatures of 700–800 °C. Aluminum oxide nanoparticles were wholly wetted by aluminum and uniformly distributed over the “in situ” metal volume. The concentration of 100 nm Al₂O₃ particles formed inside the aluminum matrix depended entirely on the exposure time and concentration of titanium dioxide in the melt. The mass fraction of aluminum oxide in the composite may have been increased up to 19 wt.%.

Melting temperatures of composites with 4–19 wt.% of nano- α - Al₂O₃ did not differ from the aluminum melting point because of the uniform distribution of nanometer alumina inclusions in the composites.

It was revealed that the tensile strength, yield strength, hardness, and ductility of cast Al- α -nano-Al₂O₃ composites in uniaxial tension increased up to 20–30% in the presence of α -Al₂O₃ nanoparticles in the structure of aluminum. The tensile strength reached maximum for the composites with 14 wt.% of α -nano-Al₂O₃, and it was the same for those with 19 wt.% of α -nano-Al₂O₃. This remarkable improvement of tensile strength was accompanied by a significant simultaneous increase in the elongation of nanocomposite by three times as opposed to the initial aluminum. The reason for such a combination of mechanical properties was the formation of very small nanoparticles of α -Al₂O₃ that were fully wetted and uniformly distributed in the aluminum matrix.

Composite materials of the Al-Al₂O₃ system could be easily rolled into thin and ductile foils and wires.

Thus, the formed metal composite materials of the Al-Al₂O₃ system combined the advantages of a low-melting metal matrix and the properties of a ceramic dispersive filler α -Al₂O₃, which makes this system an extremely attractive structural material, that is very light, strong, hard, and elastic.

A possible mechanism for the simultaneous increase in mechanical properties and elongation in tension when true aluminum oxide nanoparticles are introduced into the Al-Al₂O₃ composite will be the subject of our further study.

Author Contributions: Data curation, L.A.Y.; Formal analysis, L.A.Y.; Investigation, A.G.K., D.I.V. and E.O.S.; Methodology, L.A.Y.; Writing—original draft, L.A.Y. All authors have read and agreed to the published version of the manuscript.

Funding: The work was funding by the Research Program № 122020100210-9 (IHTE UB RAS), Russian Academy of Sciences, Ural Branch, Russia.

Institutional Review Board Statement: Not applicable.

Informed Consent Statement: Not applicable.

Data Availability Statement: Not applicable.

Acknowledgments: This work was carried out using equipment at the Shared Access Center for the Composition of Compounds, Institute of High-Temperature Electrochemistry, Ural Branch, RAS (Ekaterinburg, Russia) for analytical support and the Shared Access Centre “Plastometry”, Institute of Engineering Science, Ural Branch, RAS (Ekaterinburg, Russia) for mechanical testing.

Conflicts of Interest: The authors declare that they have no known competing financial interest or personal relationships that could have appeared to influence the work reported in this paper.

References

1. Srivastava, N.; Chaudhari, G.P. Strengthening in Al alloy nanocomposites fabricated by ultrasound assisted solidification technique. *Mater. Sci. Eng. A* **2016**, *651*, 241–247. [[CrossRef](#)]
2. Yolshina, L.A.; Muradymov, R.V.; Vichuzhanin, D.I.; Smirnova, E.O. Enhancement of the mechanical properties of aluminum-graphene composites. *AIP Conf. Proc.* **2016**, *1785*, 040093. [[CrossRef](#)]
3. Gaitonde, V.N.; Karnik, S.R.; Jayaprakash, M.S. Some Studies on Wear and Corrosion Properties of Al5083/Al₂O₃/Graphite Hybrid Composites. *J. Miner. Mater. Charact. Eng.* **2012**, *11*, 695–703.

4. Schultz, B.F.; Ferguson, J.B.; Rohatgi, P.K. Microstructure and hardness of Al₂O₃ nanoparticle reinforced Al–Mg composites fabricated by reactive wetting and stir mixing. *Mater. Sci. Eng. A* **2011**, *530*, 87–97. [[CrossRef](#)]
5. Chikova, O.A.; Finkelstein, A.B.; Schaefer, A. Microstructures, mechanical properties ingot AlSi7Fe1 after blowing oxygen through melt. *Acta Metall. Slovaca. B* **2017**, *23*, 4–11.
6. Karnesky, R.A.; Meng, L.; Dunand, D.C. Strengthening mechanisms in aluminum containing coherent Al₃Sc precipitates and incoherent Al₂O₃ dispersoids. *Acta Mater.* **2007**, *55*, 1299–1308. [[CrossRef](#)]
7. Su, H.; Gao, W.; Feng, Z.; Lu, Z. Processing, microstructure and tensile properties of nano-sized Al₂O₃ particle reinforced aluminum matrix composites. *Mater. Des.* **2012**, *36*, 590–596. [[CrossRef](#)]
8. Luan, B.F.; Hansen, N.; Godfrey, A.; Wu, G.H.; Liu, Q. High strength Al–Al₂O₃p composites: Optimization of extrusion parameters. *Mater. Des.* **2011**, *32*, 3810–3817. [[CrossRef](#)]
9. Hamid, A.A.; Ghosh, P.K.; Jain, S.C.; Ray, S. The influence of porosity and particles content on dry sliding wear of cast in situ Al(Ti)–Al₂O₃(TiO₂) composite. *Wear* **2008**, *265*, 14–26. [[CrossRef](#)]
10. Shafiei-Zarghani, A.; Kashani-Bozorg, S.F.; Zarei-Hanzaki, A. Microstructures and mechanical properties of Al/Al₂O₃ surface nano-composite layer produced by friction stir processing. *Mater. Sci. Eng. A* **2009**, *500*, 84–91. [[CrossRef](#)]
11. Kok, M.; Ozdin, K. Wear resistance of aluminium alloy and its composites reinforced by Al₂O₃ particles. *J. Mater. Processing Technol.* **2007**, *183*, 301–309. [[CrossRef](#)]
12. Azarniya, A.; Hosseini, H.R.M.; Jafari, M.; Bagheri, N. Thermal decomposition of nanostructured Aluminum Titanate in an active Al matrix: A novel approach to fabrication of in situ Al/Al₂O₃–Al₃Ti composites. *Mater. Des.* **2015**, *88*, 932–941. [[CrossRef](#)]
13. Tong, X.C.; Fang, H.S. Al–TiC Composites In Situ–Processed by Ingot Metallurgy and Rapid Solidification Technology: Part I. Microstructural Evolution. *Metall. Mater. Trans. A* **1998**, *29*, 875–891. [[CrossRef](#)]
14. Yolshina, L.A.; Muradymov, R.V.; Korsun, I.V.; Yakovlev, G.A.; Smirnov, S.V. Novel aluminum-graphene and aluminum-graphite metallic composite materials: Synthesis and properties. *J. Alloys Compd.* **2016**, *663*, 449–459. [[CrossRef](#)]
15. Yadav, M.; Kumaraswamidhas, L.A.; Singh, S.K. Investigation of solid particle erosion behavior of Al–Al₂O₃ and Al–ZrO₂ metal matrix composites fabricated through powder metallurgy technique. *Tribol. Int.* **2022**, *172*, 107636. [[CrossRef](#)]
16. Zhang, Z.; Fan, G.; Tan, Z.; Zhao, H.; Xu, Y.; Xiong, D.; Li, Z. Towards the strength-ductility synergy of Al₂O₃/Al composite through the design of roughened interface. *Compos. Part B* **2021**, *224*, 109251. [[CrossRef](#)]
17. Liu, J.; Cao, G.; Zhu, X.; Zhao, K.; An, L. Optimization of the microstructure and mechanical properties of heterogeneous Al–Al₂O₃ nanocomposites. *Mater. Today Commun.* **2020**, *25*, 101199. [[CrossRef](#)]
18. Han, Q.; Setchi, R.; Evans, S.L. Synthesis and characterisation of advanced ball-milled Al–Al₂O₃ nanocomposites for selective laser melting. *Powder Technol.* **2016**, *297*, 183–192. [[CrossRef](#)]
19. Liu, J.; Huang, X.; Zhao, K.; Zhu, Z.; Zhu, X.; An, L. Effect of reinforcement particle size on quasistatic and dynamic mechanical properties of Al–Al₂O₃ composites. *J. Alloys Compd.* **2019**, *797*, 1367–1371. [[CrossRef](#)]
20. Vogel, T.; Ma, S.; Liu, Y.; Guo, Q.; Zhang, D. Impact of alumina content and morphology on the mechanical properties of bulk nanolaminated Al₂O₃–Al composites. *Compos. Commun.* **2020**, *22*, 100462. [[CrossRef](#)]
21. Liu, W.; Ke, Y.; Sugio, K.; Liu, X.; Guo, Y.; Sasaki, G. Microstructure and mechanical properties of Al₂O₃-particle-reinforced Al-matrix composite sheets produced by accumulative roll bonding (ARB). *Mater. Sci. Eng. A* **2022**, *850*, 143574. [[CrossRef](#)]
22. Sadeghi, B.; Cavaliere, P.; Balog, M.; Pruncu, C.I.; Shabani, A. Microstructure dependent dislocation density evolution in micro-macro rolled Al₂O₃/Al laminated composite. *Mater. Sci. Eng. A* **2022**, *830*, 142317. [[CrossRef](#)]
23. Gao, T.; Liu, L.; Liu, G.; Liu, S.; Li, C.; Li, M.; Zhao, K.; Han, M.; Wu, Y.; Liu, X. In-situ synthesis of an Al-based composite reinforced with nanometric γ -Al₂O₃ and submicron AlB₂ particles. *J. Alloys Compd.* **2022**, *920*, 165985. [[CrossRef](#)]
24. Tjong, S.C.; Ma, Z.Y. Microstructural and mechanical characteristics of in situ metal matrix composites. *Mater. Sci. Eng.* **2000**, *29*, 49–113. [[CrossRef](#)]
25. Zhao, Y.; Zhang, S.; Chen, G. Aluminum matrix composites reinforced by in situ Al₂O₃ and Al₃Zr particles fabricated via magnetochemistry reaction. *Trans. Nonferrous Met. Soc. China* **2010**, *20*, 2129–2133. [[CrossRef](#)]
26. Elshina, L.A.; Muradymov, R.V.; Kvashnichev, A.G.; Vichuzhanin, D.I.; Molchanova, N.G.; Pankratov, A.A. Synthesis of new metal-matrix Al–Al₂O₃–graphene composite materials. *Russ. Metall. (Met.)* **2017**, *2017*, 631–641. [[CrossRef](#)]
27. Elshina, L.A.; Kudjakov, V.Y.; Malkov, V.B.; Elshin, A.N. High-Temperature Electrochemical Synthesis of Oxide Thin Films and Nanopowders of Some Metal Oxides. *Glass Phys. Chem.* **2008**, *34*, 617–622. [[CrossRef](#)]
28. Elshina, L.A.; Kvashnichev, A.G.; Pelegov, D.V. Electrochemical Synthesis of Titanium Oxide Nanopowders in a Molten Mixture of Alkali Chlorides and Nitrates. *Russ. Metall. (Met.)* **2021**, *2021*, 1029–1035. [[CrossRef](#)]
29. Savrai, R.A.; Skorynina, P.A.; Makarov, A.V.; Osintseva, A.L. Effect of Liquid Carburizing at Lowered Temperature on the Micromechanical Characteristics of Metastable Austenitic Steel. *Phys. Met. Metallogr.* **2020**, *121*, 1015–1020. [[CrossRef](#)]
30. Cheng, Y.T.; Cheng, C.M. Relationships between hardness, elastic modulus and the work of indentation. *Appl. Phys. Lett.* **1998**, *73*, 614–618. [[CrossRef](#)]
31. Petrzhik, M.I.; Levashov, E.A. Modern methods for investigating functional surfaces of advanced materials by mechanical contact testing. *Crystallogr. Rep.* **2007**, *52*, 966–974. [[CrossRef](#)]
32. Mayrhofer, P.H.; Mitterer, C.; Musil, J. Structure-property relationships in single- and dual-phase nanocrystalline hard coatings. *Surf. Coat. Technol.* **2003**, *174–175*, 725–731. [[CrossRef](#)]

33. Yolshina, L.A.; Kudyakov, V.Y.; Malkov, V.B.; Molchanova, N.G. Corrosion and electrochemical behavior of aluminium treated with high-temperature pulsed plasma in CsCl-NaCl-NaNO₃ melt. *Corros. Sci.* **2011**, *53*, 2015–2026. [[CrossRef](#)]
34. Yolshina, L.A.; Malkov, V.B.; Yolshin, A.N. The influence of formation conditions on the electrochemical behavior of lead oxide in sulfuric acid solution. *J. Power Sources* **2009**, *191*, 36–41. [[CrossRef](#)]
35. Ijadpanah-Saravy, H.; Safari, M.; Khodadadi-Darban, A.; Rezaei, A. Synthesis of titanium dioxide nanoparticles for photocatalytic degradation of cyanide. *Anal. Lett.* **2014**, *47*, 1772–1782. [[CrossRef](#)]
36. Yolshina, L.A.; Kvashinchev, A.G. Chemical Interaction of Liquid Aluminum with Metal Oxides in Molten Salts. *Mater. Des.* **2016**, *105*, 124–132. [[CrossRef](#)]
37. Yolshina, L.A.; Kvashinchev, A.G.; Pelegov, D.V.; Pryakhina, V.I. Molten salt synthesis and characterization of 1D sodium hexatitanate nanowires. *Colloids Interface Sci. Commun.* **2021**, *42*, 100398. [[CrossRef](#)]
38. Elshina, L.A.; Elshina, V.A. Synthesis of a Nanocrystalline α -Al₂O₃ Powder in Molten Halides in the Temperature Range 700–800 °C. *Russ. Metall. (Met.)* **2020**, *2020*, 138–141. [[CrossRef](#)]
39. Batyshev, A.I. *Crystallization Metals and Alloys Under Pressure*; Kristallizatsia Metallov i Splavov Pod Davleniem; Metallurgy: Moscow, Russia, 1977; 151p.
40. Hossein-Zadeh, M.; Razavi, M.; Mirzaee, O.; Ghaderi, R. Characterization of properties of Al–Al₂O₃ nano-composite synthesized via milling and subsequent casting. *J. King Saud Univ. Eng. Sci.* **2013**, *25*, 75–80. [[CrossRef](#)]
41. Vorozhtsov, S.A.; Zhukov, I.A.; Vorozhtsov, A.B.; Zhukov, A.S.; Eskin, D.G.; Kvetinskaya, A.V. Synthesis of Micro- and Nanoparticles of Metal Oxides and Their Application for Reinforcement of Al-Based Alloys. *Adv. Mater. Sci. Eng.* **2015**, *2015*, 718207. [[CrossRef](#)]
42. Dang, X.; Zhang, B.; Zhang, Z.; Hao, P.; Xu, Y.; Xie, Y. Microstructural evolutions and mechanical properties of multilayered 1060Al/Al–Al₂O₃ composites fabricated by cold spraying and accumulative roll bonding. *J. Mater. Res. Technol.* **2021**, *15*, 3895–3907. [[CrossRef](#)]
43. Ma, P.; Jia, Y.; Gokuldoss, P.K.; Yu, Z.; Yang, S.; Zhao, J.; Li, C. Effect of Al₂O₃ Nanoparticles as Reinforcement on the Tensile Behavior of Al–12Si Composites. *Metals* **2017**, *7*, 359. [[CrossRef](#)]